PERGAMON

International Journal of Mechanical Sciences 43 (2001) 715–742

International Journal of MECHANICAL SCIENCES

www.elsevier.com/locate/ijmecsci

Cold compaction of an array of cylindrical fibres

I. Sridhar[a], N.A. Fleck[a,*], A.R. Akisanya[b]

[a]*Department of Engineering, University of Cambridge, Trumpington Street, Cambridge, CB2 1PZ, UK*
[b]*Department of Engineering, University of Aberdeen, Aberdeen, AB24 3UE, UK*

Received 9 August 1999; received in revised form 25 February 2000

Abstract

The biaxial compaction of a square array of circular cylinders is studied using slip-line field, upper bound and finite element methods. Densification is assumed to occur by plastic deformation at the contacts. It is found that contact–contact interaction has a softening effect on the local indentation pressure at each contact. The yield surfaces resulting from hydrostatic and closed-die compaction are constructed at various stages of densification: the size and shape of the yield surface depend upon the loading history and upon the relative density of the compact. The finite element predictions suggest the formation of a vertex at the loading point for the entire densification process in the case of isostatic compaction. On the other hand, a vertex at the loading point is formed only for a relative density $D \leqslant 0.85$ in the case of closed-die compaction.

Keywords: Powder compaction; Yield surface; Slip-line field method; Upper bound methods; Finite element method

1. Introduction

Powder compaction is a popular net shape forming operation for small, high volume engineering parts. Powder metallurgy materials include refractory metals, superalloys, particle and fibre-reinforced composites, ferrous alloys and cermets. The ability to control accurately the size, composition and morphology of the microstructure is a major advantage of the powder route. Cold compaction followed by sintering avoids the segregation and excessive grain growth associated with casting. When the operating temperature is less than 0.3 times the absolute melting point of the metal, rate-independent plasticity is the dominant mechanism of densification. At higher temperatures densification is assisted by creep and diffusional flow.

* Corresponding author. Tel.: + 44-01223-332650; fax: 0044-1223-332662.
E-mail address: naf1@eng.cam.ac.uk (N.A. Fleck).

0020-7403/01/$ - see front matter
PII: S0020-7403(00)00037-0

The starting powder for a compaction process typically consists of randomly oriented loose particles with a wide range of particle size and shape. Three different stages of powder compaction may be identified as follows. Stage 0 is the initial rearrangement of powder particles. For equi-sized spherical particles, this initial rearrangement results in a relative density of about 0.64 [1], where the relative density is defined as the ratio of the average density of the powder to that of the fully dense solid. In the second stage, Stage I, particles indent each other at isolated necks, leaving a network of inter-connected porosity. Densification occurs by the mutual indentation of particles in contact, with the continuous growth of interparticle necks. Helle et al. [2] argue that this geometrical description prevails up to a relative density of about 0.9. In the final stage (Stage II), the relative density is greater than 0.9, and the interparticle necks have grown until the porosity pinches off into isolated voids. The compact at this stage is modelled as a porous solid and densification is controlled by the shape, size and distribution of the pores.

Doraivelu et al. [3] have summarised the macroscopic yield surfaces from several Stage I and Stage II powder compaction models by adopting the following quadratic form:

$$f_1(D)\sigma_m^2 + f_2(D)\sigma_e^2 = \sigma_Y^2, \tag{1}$$

where f_1 and f_2 are functions of relative density D, σ_m is the mean stress, σ_e is the von Mises effective stress, and σ_Y is the uniaxial yield strength of the matrix. Brown and Abou-Chedid [4] have measured the isodensity curves in stress space for copper and iron powders compacted under biaxial and triaxial states of stress. They observed a lack of correspondence between the isodensity curves and the yield surface of the form given by Doraivelu et al. [3]. This discrepancy between the yield functions of form (1) and various experimental data implies that the yield behaviour of a powder aggregate does not depend on density alone, but also depends upon the loading path. In an anisotropic model for Stage I compaction of spherical particles, Fleck [5] has estimated the distribution of contacts and the variation of the size of the contacts in terms of a second-order tensor B_{ij}, which is closely related to the macroscopic strain E_{ij}. The macroscopic yield surface depends upon the loading path used for the compaction, and a vertex is observed at the loading point. Storakers et al. [6] have extended this approach for powder composites undergoing power law visco-plastic compaction. Akisanya et al. [7] have measured the sensitivity of the yield surface shape to the deformation path by conducting triaxial tests on copper powder. The observed yield surface is elongated along the loading direction with a vertex at the loading point for closed-die compaction, and lends support to the models of Fleck [5] and Storakers et al. [6].

An accurate prediction of powder compaction in Stages I and II requires a knowledge of the contact pressure between individual particles, and of the number of contacts Z per particle. Early studies of Stage I cold compaction of powder particles assumed a constant contact pressure, but an increasing number of contacts during the initial stages of densification. Helle et al. [2] used Prandtl's punch solution of an infinite solid and Fleck et al. [8] used the solution given by Green [9] for the plastic yielding of a metal junction under combined shear and pressure. But compression experiments on single spherical metal particles reveal that the mean pressure at the neck between two particles falls with increasing neck size [10,11]. With increasing compaction, the plastic zone at each contact interacts with those of neighbouring contacts or with the free surface of the particles [12,13] and gives rise to reduced contact pressures.

Next, consider the evolution of co-ordination number Z with relative density, D. A dense random packing of aligned, monosized cylindrical particles typically has a starting relative density

of between 75 and 80% [14]. This corresponds to an average number of contacts per particle (that is, the particle co-ordination number, Z) of 3–4. For random packing, Z increases during densification from about 4 to a maximum of 6. Two limiting particle arrangements for the cylindrical particle array are a square array corresponding to a low initial relative density ($D_0 = 0.7854$) with particle co-ordination number, $Z = 4$, and a hexagonal close-packed arrangement corresponding to a high relative density ($D_0 = 0.9068$) with $Z = 6$. Akisanya et al. [12] have used slip-line field and finite element methods to study the pressure versus density response of regular hexagonal array of cylindrical particles. Subsequently, they used these methods to determine Stage I yield surface for hydrostatic and closed-die precompacts [15].

In the current study we analyse Stage I and Stage II cold compaction of square arrays of circular cylindrical particles, as a prototype for the more complex case of three-dimensional compaction of non-prismatic particles. Additionally, the study is motivated by the practical problem of the compaction of aligned layers of metallic fibres in metal matrix composite manufacture [16]. Initially, we present a brief description of the methods employed. Then, Stage I and Stage II hydrostatic compaction are examined using slip-line field and finite element methods. The macroscopic stress–strain response for general loading and the effect of material strain-hardening on the pressure–density response are investigated using the finite element method. The shape and size of the yield surface are determined at various stages of densification for both hydrostatic and closed-die compaction using slip-line field, upper bound and finite element methods.

2. Modelling details

The arrangement of particles adopted in this study is shown in Fig. 1. It consists of a square array of identical circular cylindrical particles of initial radius R_0. The compaction response will be discussed in terms of a representative unit cell, comprising one-quarter of a cylinder and pore, with two contacts. The relative density D is defined as the ratio of the area of the solid material in the unit cell to the area of the unit cell. Thus, the initial relative density is $D_0 = \pi/4 = 0.7854$. Fleck [5] has shown that inter-particle friction plays only a minor role in Stage I compaction, and so we assume frictionless contacts throughout this study. In fact, the particle arrangements adopted in

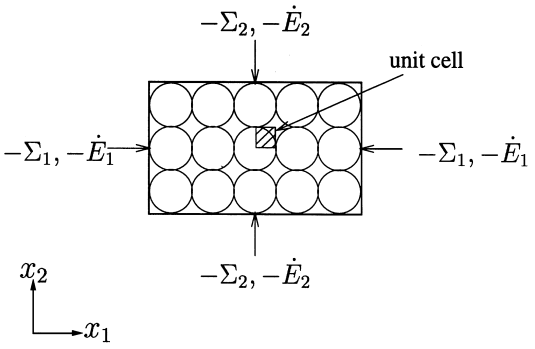

Fig. 1. Sketch of a square arrangement of circular cylindrical fibres of radius R_0, subjected to macroscopic compressive loading $-\Sigma_1$ and $-\Sigma_2$. The work-conjugate plastic strain rate is $-\dot{E}_1$ and $-\dot{E}_2$.

this study automatically result in zero shear traction at contacts. Additionally, the contacts are assumed to possess zero cohesive (tensile) strength; these assumptions are reasonable for the practical problem of the cold compaction of lubricated metallic powders.

As for the case of compaction of spherical particles, the compaction process of cylindrical particles can be divided into Stages I and II. During the initial stage (Stage I), the individual cylindrical particles are still recognisable and plastic deformation is localised near the contacts. In the later stages of densification the plastic fields from neighbouring contacts interact and the pores are cusped in shape: this stage is the *interaction* stage. In the final stages of densification (Stage II) the pores formed between the contacting particles are surrounded by a zone of plastically deforming material. At this stage the geometry is modelled as an array of pores which shrink in size as densification progresses.

2.1. Finite element analysis

Since the cylindrical particles are allowed to slide freely past each other, the deformation can be modelled by considering the indentation of a long cylinder by a smooth flat punch. The problem is to obtain the macroscopic Cauchy stress (Σ_1, Σ_2) for the square arrangement of identical cylindrical particles subjected to a plane strain deformation state, characterised by the logarithmic strain measures (E_1, E_2), in terms of the Cartesian axes (x_1, x_2) shown in Fig. 1.

The finite element package ABAQUS[1] is used for the numerical calculations for the entire compaction process (Stages I and II); a finite strain version of J2 flow theory is used to describe the constitutive response of the matrix. Unless otherwise stated, the governing stress–strain response of the cylindrical particles is assumed to be an elastic-perfectly plastic solid with a yield strain of 10^{-4} and a Poisson's ratio of $\nu = 0.3$. As the finite element results will be compared with rigid, ideally plastic slip-line field and upper bound solutions, we have chosen a small value of yield strain in FE analysis. Preliminary calculations confirm that the compaction results are insensitive to the choice of yield strain.

The assumed symmetry with respect to both geometry and loading implies that it is adequate to model only one-quarter of a particle, as shown in Fig. 2. The mesh in Fig. 2 consists of 1448 quadratic and 884 triangular plane strain-reduced integration elements. The vertical and horizontal symmetry boundaries of the unit cell are subjected to displacement boundary conditions in which elements are allowed to slide freely along the boundary with zero shear traction. In order to simulate plane strain compaction, normal displacements are imposed along the top and right-hand side of the representative unit cell using frictionless interface elements. The curved surface of the particle is traction-free.

The evolution of the contact width parameters (a_1, a_2), the centre distances between the neighbouring particles (b_1, b_2) and the total reaction force at each contact is determined as a function of the macroscopic strain (E_1, E_2), see Fig. 3(a). The macroscopic response of the aggregate is given by the average state of stress and strain in the representative unit cell. We note that the macroscopic logarithmic strain is related to the particle spacings $(2b_1, 2b_2)$ and

[1] ABAQUS, HKS Inc., RI, USA.

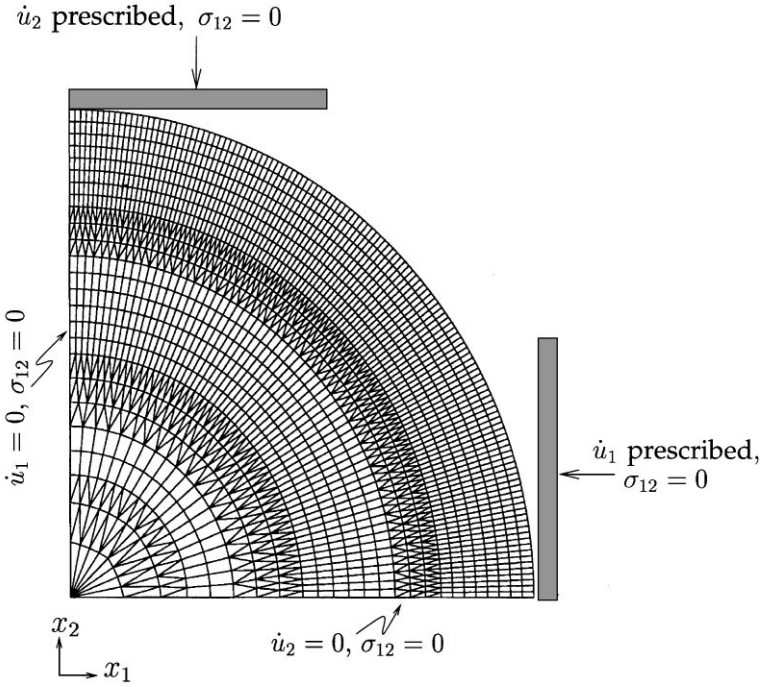

Fig. 2. Finite element mesh of a unit cell of the square array showing the boundary conditions and loading.

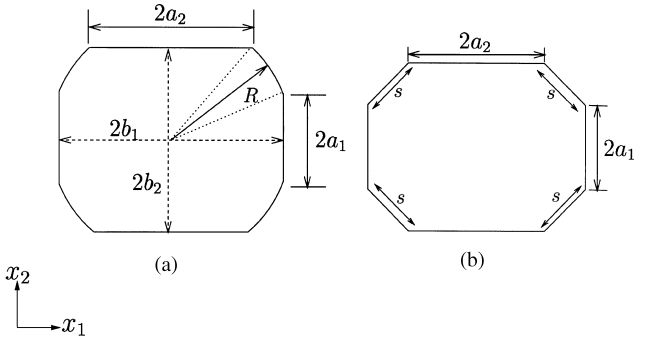

Fig. 3. Assumed particle geometry for: (a) Stage I compaction; and (b) Stage II compaction, for slip-line field and upper bound methods. The free surface of the particles are assumed to have a uniform radius of curvature R in Stage I, whereas the voids are taken to be square with a side length s in Stage II.

to the radius of the undeformed particle R_0 by

$$E_1 = \ln\left(\frac{b_1}{R_0}\right), \tag{2}$$

$$E_2 = \ln\left(\frac{b_2}{R_0}\right) \tag{3}$$

and the relative density D is related directly to the strain state (E_1, E_2) by

$$\ln\left(\frac{D}{D_0}\right) = -(E_1 + E_2) \tag{4}$$

where D_0 is the initial relative density, as defined previously. The total reaction force at each contact is divided by the contact width to obtain the mean contact pressures p_1 and p_2. By equilibrium, the macroscopic stresses are related to the inter-particle contact pressure p_1 and p_2 at the contacts along the x_1 and x_2 axes by

$$\Sigma_1 = -\left(\frac{a_1}{b_2}\right)p_1, \tag{5}$$

$$\Sigma_2 = -\left(\frac{a_2}{b_1}\right)p_2. \tag{6}$$

2.2. Approximate geometric relations for slip-line field and upper bound methods

The slip-line and upper bound methods assume a rigid, ideally plastic material response. In order to specify the evolution of contact size between particles, as a function of macroscopic strain, a number of additional geometrical assumptions are required as follows.

Stage I: When the square array of particles are subjected to macroscopic loading, the particle centres approach each other and finite contacts form between the particles. Deformation is confined to the regions of the contact during the early stages of compaction. As the powder particles are compacted further the plastic field interacts between the contacts and the particle's free surface; material is extruded from beneath the contacts into the adjacent voids. The extruded material from the contact is assumed to be distributed uniformly over the free surface of the particle so that the free surface of the particle has a radius $R > R_0$. In this way, the contacts grow as the relative density increases. This assumption also ensures that the pores in the powder structure remain cusped in shape.

A typical deformed shape of a particle under applied macroscopic strain state (E_1, E_2) is illustrated in Fig. 3(a). The contacts appear as flat faces on each particle. The local deformation of a particle is characterised by the contact widths $2a_1$ and $2a_2$ and by the centre distance between the particles $2b_1$ and $2b_2$ along x_1- and x_2-directions, respectively. The contact widths are related to the current particle radius R by the following equations:

$$a_1^2 + b_1^2 = R^2, \tag{7}$$

$$a_2^2 + b_2^2 = R^2. \tag{8}$$

By conservation of volume, the cross-sectional area of each cylindrical particle at any stage of deformation equals the initial cross-sectional area of the undeformed particle of radius R_0, giving

$$\left(\frac{R_0}{R}\right)^2 = 1 + \frac{2}{\pi}\left[\frac{a_1}{b_1}\left(1 + \frac{a_1^2}{b_1^2}\right)^{-1} + \frac{a_2}{b_2}\left(1 + \frac{a_2^2}{b_2^2}\right)^{-1} - \tan^{-1}\left(\frac{a_1}{b_1}\right) - \tan^{-1}\left(\frac{a_2}{b_2}\right)\right]. \tag{9}$$

The relative density D can therefore be shown to be

$$D = \frac{1}{2}\left(\frac{a_1}{b_2} + \frac{a_2}{b_1}\right) + \frac{1}{2}\left(1 + \frac{a_1^2}{b_1^2}\right)^{1/2}\left(1 + \frac{a_2^2}{b_2^2}\right)^{1/2}\left[\frac{\pi}{2} - \tan^{-1}\left(\frac{a_1}{b_1}\right) - \tan^{-1}\left(\frac{a_2}{b_2}\right)\right]. \tag{10}$$

The center spacings $2b_1$ and $2b_2$ evolve with macroscopic strain (E_1, E_2) according to relations (2) and (3). We now have a complete set of relations (2), (3), (7)–(10) in order to obtain the geometric parameters $(a_1, a_2, b_1, b_2, R, D)$ as a function of the macroscopic strain (E_1, E_2), initial particle radius R_0 and initial relative density D_0. Expression (4) for D is mathematically identical to Eq. (10) since both are statements of conservation of mass. The connection (5) and (6) between the macroscopic stress (Σ_1, Σ_2) and the average contact pressures (p_1, p_2) apply also for the slip-line field and upper bound methods.

Stage II: In Stage II densification, plastic deformation occurs in the vicinity of each pore, and the pore is treated as a square of side length s in order to simplify the slip-line field and upper bound analysis, see Fig. 3(b). An expression for relative density can be easily deduced from conservation of mass and is given by

$$D = 1 - \frac{1}{2}\left(1 - \frac{a_1}{b_2}\right)\left(1 - \frac{a_2}{b_1}\right). \tag{11}$$

3. Hydrostatic compaction

In this section, we study the evolution of contact size, mean contact pressure and the macroscopic pressure for the hydrostatic compaction of a square array of cylindrical particles using the finite element and slip-line field methods. When the macroscopic stress is hydrostatic, we may write $\Sigma_1 = \Sigma_2 = \Sigma_m$, and symmetry dictates that only $\frac{1}{8}$ of a representative particle needs to be considered.

3.1. Contact size evolution

For hydrostatic compaction the contact widths are of equal size $a_1 = a_2 = a$ and $b_1 = b_2 = b$. In the finite element (FE) calculations, the contact widths are measured from the deformed shape of the particle and the relative density D is calculated directly from the macroscopic strain via relation (4). The computed variation of relative density D with the contact size a/b is shown in Fig. 4.

The approximate geometrical relation (10) is used in the slip-line field (and upper bound calculations) in order to relate D to a/b, giving for Stage I hydrostatic compaction,

$$D = \frac{a}{b} + \left(1 + \frac{a^2}{b^2}\right)\left[\frac{\pi}{4} - \tan^{-1}\left(\frac{a}{b}\right)\right]. \tag{12}$$

In Stage II, the size s of square pore is related to the contact size a by

$$\frac{a}{b} = 1 - \frac{1}{\sqrt{2}}\frac{s}{b} \tag{13}$$

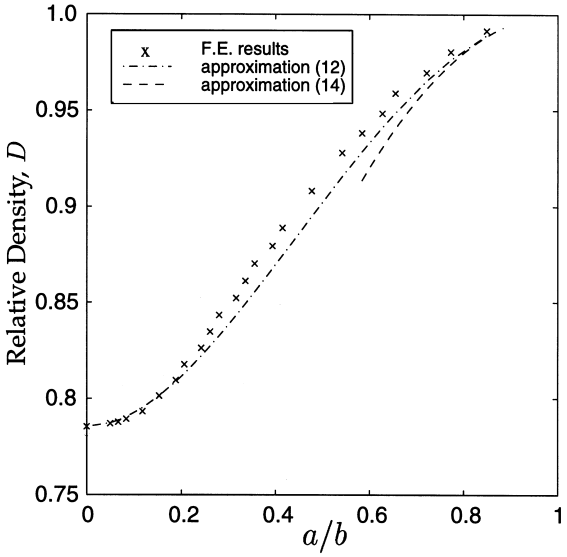

Fig. 4. Comparison of the analytical predictions (12) and (14) with the finite element results, for the evolution of contact size with relative density, D.

and the relative density D follows as

$$D = 1 - \frac{1}{2}\left(1 - \frac{a}{b}\right)^2. \tag{14}$$

Predictions (12) and (14) for the relative density D are plotted as a function of contact width a/b in Fig. 4. The agreement between the approximate analytical prediction and the finite element simulation of contact size is excellent for Stage I and is adequate for Stage II.

3.2. The evolution of local contact pressure in hydrostatic compaction

The finite element predictions for the local contact pressure versus the normalised contact width a/b are plotted in Fig. 5(a). We found that the mesh discretization leads to high contact loads (p/σ_Y greater than 2.97) at small contact sizes. The average contact pressure drops due to contact–contact interaction (up to $a/b \simeq 0.58$) but starts to increase thereafter. This is due to the fact that the material displaced under the contact is forced to extrude through the decreasing gap between the neighbouring contacts: highly constrained plastic flow occurs. This has been referred to as "geometrical hardening" in the literature [17].

Next, we compare the finite element predictions with slip-line field solutions. At the start of densification, when the contacts are much smaller than the particle radius, the deformation is concentrated at the particle contacts and there is no interaction between contacts. The slip-line solution at this stage of deformation is the Prandtl indentation field. A triangular zone of dead material adheres to the punch and moves as a rigid body with the punch as shown in Fig. 6(a). The

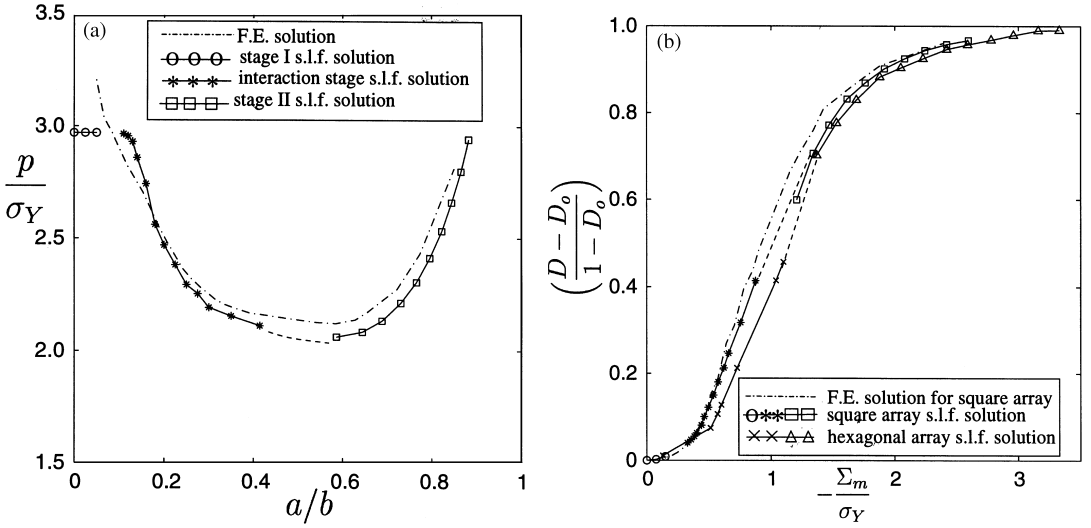

Fig. 5. (a) The mean contact pressure at the contacts versus the normalised contact width a/b for hydrostatic compaction of a square array of particles. Predictions are compared from the finite element (F.E.) method and from the slip-line field (s.l.f.) method. (b) The normalised hydrostatic pressure Σ_m/σ_Y versus the relative density. Slip-line field (s.l.f.) solutions are shown for a hexagonal array and a square array.

uniform pressure on the punch is given by Prandtl's solution $p = [(2 + \pi)/\sqrt{3}]\sigma_Y = 2.97\sigma_Y$, where p is the local pressure at each contact and σ_Y is the uniaxial yield strength.

As densification proceeds, the contact size increases, the distance between neighbouring contacts decreases and the contacts begin to interact when the contact size is no longer small compared to the distance between the contacts. A typical slip-line field displaying such interaction is shown in Fig. 6(b). This field is similar to the one given by Johnson [18] for the forging of a cylindrical bar by V-shaped anvils. A triangular zone of dead material is attached to the punch surface and the nets of orthogonal slip lines originating from the punch corner intersect the axis of symmetry at 45°. The material in the centre of the indented cylinder is rigid while that on the outer side of the slip lines moves as a rigid body outward along the axis of symmetry. The uniform pressure on the punch surface is evaluated using the Hencky equations [19] and the condition that the net force on the zone of dead material along the axis of symmetry between neighbouring punches is zero. The pressure p is given by $p = \sigma_Y f(a/b)$ for the case of contact–contact interaction, where f is a dimensionless function of a/b. The interaction between contacts results in a net softening of the macroscopic compaction response. Gampala et al. [20] and Mesavoric and Fleck [21] have also observed softening during the initial stages of inelastic blunting of *isolated* contacts. This softening is attributed to the finite deformation effects and to the interaction of the plastic zone with the free surface of the spherical particle.

The transition from the case of isolated contacts to that of contact–contact interaction occurs when the slip-line field of Fig. 6(b) provides a value of p/σ_Y equal to the Prandtl value of 2.97. Based on this condition, the transition occurs at a value of $a/b = 0.11$. The slip-line field is admissible provided the angle between the outermost slip-line emanating from the corner of the punch and the stress-free particle surface is greater than or equal to 45° [22]. For the present geometry,

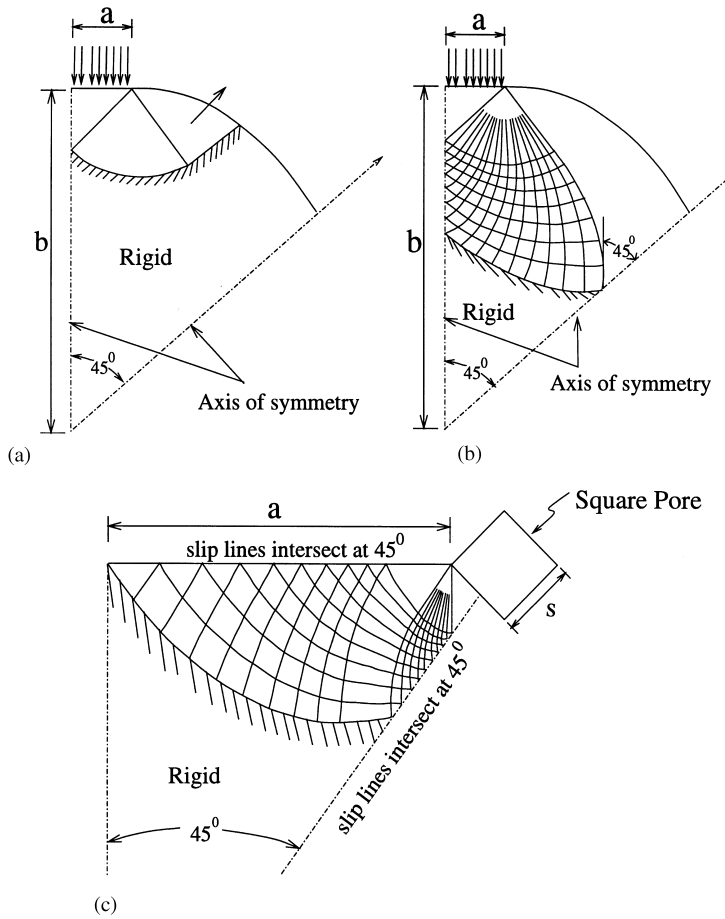

Fig. 6. The slip-line fields for hydrostatic loading ($a_1 = a_2 = a$; $b_1 = b_2 = b$): (a) Stage I with isolated contacts; (b) contact–contact interaction field; and (c) Stage II.

this condition is satisfied for values of $a/b \leqslant 0.41$. Based on this assumed mode of deformation Stage I densification terminates at $a/b = 0.41$, which corresponds to a relative density of $D = 0.87$.

The slip-line field results for the normalised contact pressure p/σ_Y are plotted in Fig. 5(a); p/σ_Y equals 2.97 for $a/b \leqslant 0.11$ (isolated contact) and it decreases with increasing contact size to a value of $p/\sigma_Y = 2.11$ at $a/b = 0.41$, due to particle contact–contact interaction.

Stage II: The slip-line field for Stage II hydrostatic compaction of a square array of voids is sketched in Fig. 6(c). A triangular zone of dead material is attached to the surface of the square pore and the centre-fan is extended to intersect the contact surface and the axis of symmetry between the contacts at 45°. Deformation is concentrated between the pore and the contact, and the material at the centre of the particle is rigid. The mode of deformation shown in Fig. 6(c) is strictly valid for values of half-contact size, a, greater than or equal to the size of the square pore of side length s. From geometric considerations the assumed field is valid for $a/b \geqslant 0.584$ and for $D \geqslant 0.91$. Therefore, the region $0.87 < D < 0.91$ is the transition stage from Stage I to II.

In contrast with Stage I behaviour, the normal pressure is not uniform across the contact in Stage II. The normalised average pressure p/σ_Y on the contact surface is included in Fig. 5(a) as a function of the relative contact size a/b. As seen from the FE calculations, the mean contact pressure increases with increasing a/b in Stage II deformation from a value of about $2.1\sigma_Y$. The slip-line field solution agrees quite closely with the finite element predictions.

3.3. The macroscopic pressure–density relation

Force equilibrium dictates that the macroscopic hydrostatic pressure, $\Sigma_1 = \Sigma_2 = \Sigma_m$ applied to the square array of cylinders is related to the average contact pressure p by

$$\Sigma_m = -\frac{a}{b}p, \tag{15}$$

where $2a$ is the contact size and $2b$ is the particle centre–centre distance, as before.

Fig. 5(b) shows the normalised macroscopic pressure $-\Sigma_m/\sigma_Y$ as a function of the normalised relative density $(D - D_0)/(1 - D_0)$ from the FE computations and slip-line field results, for the square array with $D_0 = 0.785$. These results are compared with the slip-line field solution for a hexagonal array of cylindrical particles undergoing hydrostatic compaction with $D_0 = 0.906$ [15]. For the hexagonal array, the pores are assumed to be triangular in shape during the final stages of compaction (i.e. Stage II). We conclude that the variation of macroscopic pressure with normalised relative density is almost independent of the particle arrangement.

4. Yield surface for Stage I hydrostatic compaction

In the previous section we explored the variation of contact pressure and macroscopic pressure with relative density D for the hydrostatic compaction of circular cylindrical particles. Now, the interest is in the determination of the macroscopic yield surface for a compact of given relative density. Estimates of the yield surface size and shape are given using the slip-line field, upper bound and finite element methods.

4.1. Slip-line field approach

Slip-line field methods can be used to construct the limit yield surface in p_1–p_2 space for a given value of a/b. The material composing the cylindrical particles is assumed to be rigid-perfectly plastic with a uniaxial yield strength of σ_Y.

Fig. 7 shows six possible slip-line fields that can develop within a unit cell, after compaction has occurred within Stage I. The direction of plastic strain rate dictates which of the collapse modes is active. Fields A–C are the Prandtl fields at each contact; these are appropriate when the contacts are small. Field D is obtained when a pair of opposite contacts are loaded more heavily than the adjacent contacts. This leads to the interaction of the plastic deformation zones between the opposite contacts. A similar field arises when two opposing indenters are pressed into a flat sheet; the angle of the centre-fan field is determined from the requirement that the outer slip-line must

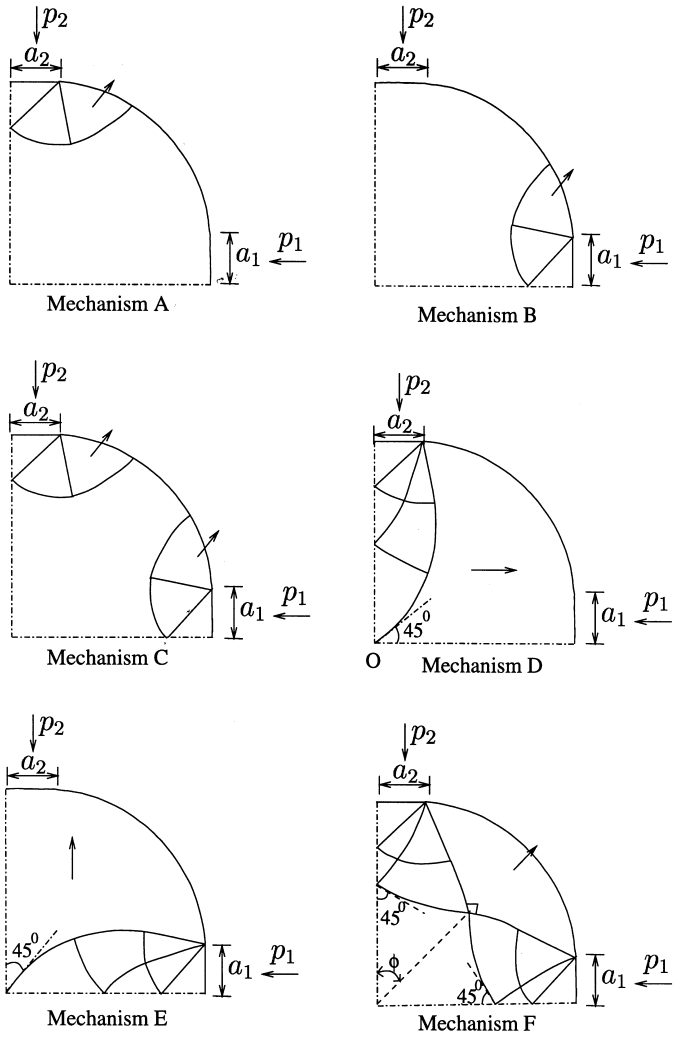

Fig. 7. Slip-line field solutions for a square array of cylindrical fibres during probing of the yield surfaces for Stage I precompacts. Six mechanisms of collapse are shown; the macroscopic strain rate direction dictates which mechanism is active.

intersect the origin O at 45° to the two axes of symmetry. The mean contact stress at the contact is determined from the equilibrium condition that the horizontal component of resultant force on the outer slip-line equals the resultant force acting on the lateral contact. The field is active only if the local contact pressure at the opposing contacts is less than the Prandtl punch value of $2.97\sigma_Y$. The deformation zone in this mechanism extends to the centre of the particle. The collapse mode E is the same as D, but with the roles of p_1 and p_2 interchanged.

Mechanism F is of the same class as the neighbouring contact–contact interaction mechanism shown in Fig. 6(b). For a given value of the angle ϕ in Fig. 7(f), the collapse state (p_1, p_2) is determined from the requirement that there is zero net force on the rigid block extruded between

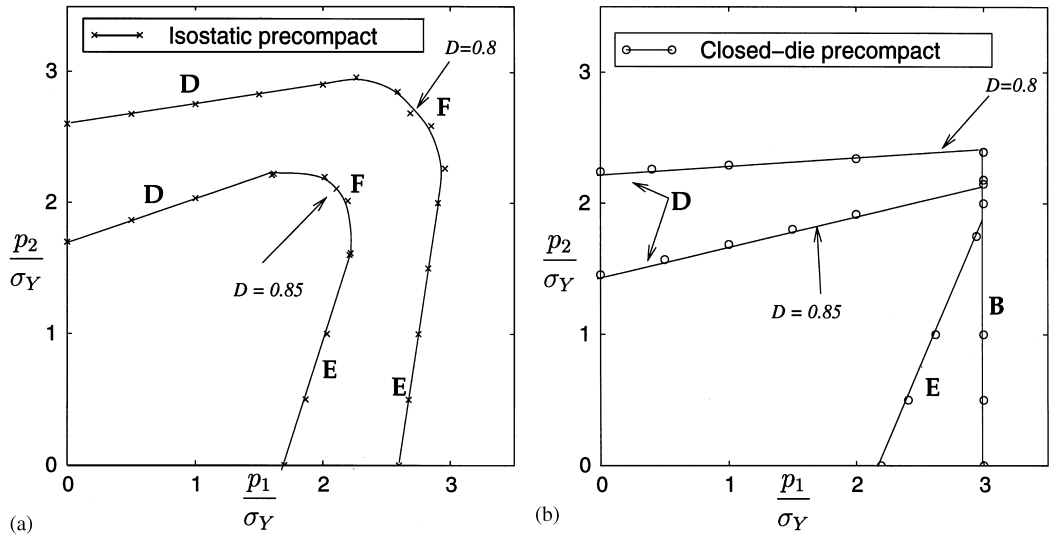

Fig. 8. Yield surfaces by the slip-line field method for: (a) isostatic precompacts; and (b) closed-die precompacts of relative densities $D = 0.8$ and 0.85. The letters **B**, **D**, **E** and **F** denote the operative mechanisms of deformation at each segment of the surfaces.

the contacts. There is a limited range of validity for the angle ϕ and therefore a limited range of possible values of p_1 and p_2 associated with this field for a precompact of given contact widths. For example, mechanism F is only valid when ϕ is in the range $33^\circ \leqslant \phi \leqslant 57^\circ$ for a hydrostatic precompact of relative density $D = 0.85$.

For each mechanism a limit surface is constructed in stress space by identifying the combinations of p_1 and p_2 required to activate that particular field. The yield surface is then obtained by the inner envelope of the limit surfaces for the individual mechanisms.

Fig. 8(a) shows the resulting yield surface for the hydrostatic precompacts of relative densities 0.8 and 0.85. The contact pressures p_1 and p_2 have been normalised by the uniaxial yield strength of the material σ_Y. For the relative densities considered, the Prandtl punch solution A gives a collapse pressure p_2 which is higher than that given by mechanism D and so mechanism A lies outside the limit surface and is discounted. Apart from mechanism F, which is the neighbouring contact–contact interaction mechanism, all the other fields produce straight lines in stress space. By using relations (5) and (6) this local yield surface can be readily converted to the macroscopic yield surface (Σ_1, Σ_2). The resulting macroscopic yield surfaces are shown in Fig. 9a for $D = 0.8$ and in Fig. 9b for $D = 0.85$. As the contacts are assumed to be cohesionless the lines $\Sigma_1 = 0$ and $\Sigma_2 = 0$ form additional boundaries of the yield surface: tensile macroscopic stresses cannot be supported by the particle aggregate. The data points on the x- and y-axis correspond to the yield strength of the compact under uniaxial free compression parallel to these axes.

4.2. Upper bound method

When the upper bound method is applied to rigid, ideally plastic solids, the assumed deformation state consists of rigid regions, sliding relative to each other. The component of material

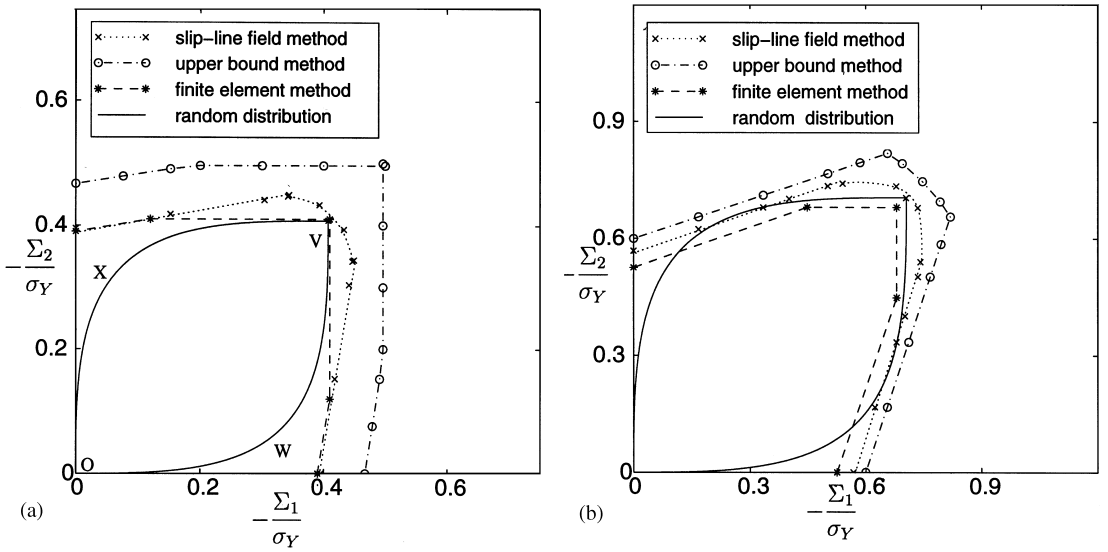

Fig. 9. Comparison of macroscopic yield surfaces for hydrostatic precompacts of: (a) relative density $D = 0.8$; and (b) relative density $D = 0.85$ using slip-line field, upper bound, random array upper bound and finite element methods.

velocity normal to each shear discontinuity is continuous by incompressibility. The accuracy of the solution depends upon the faithfulness of the assumed deformation mode to reproduce the actual solution, and the load is a minimum for the actual solution. The macroscopic consolidation stress is calculated by equating the rate of external work done to the rate of internal plastic work.

Fig. 10 shows some of the possible upper bound mechanisms that can exist within the unit cell of the cylindrical array (Fig. 1). These mechanisms are simplified versions of the slip-line fields A–F in Fig. 7. Mechanisms A and B are simple indentation fields at each contact, and are relevant when the contacts are small. These mechanisms assume that a triangular zone of dead material adheres to the contacts and moves as a rigid body with increasing deformation. The material at the centre of the particle is also rigid while the material extruded from under the contact is deposited at the edge of the contact. By neglecting the slight curvature of the particle, the minimum upper bound value of the collapse pressure can be shown to be $3.27\sigma_Y$. Mechanism C is a combination of mechanisms A and B, in which an indentation field is activated at both contacts.

In mechanism D there is an interaction between the deformation of two opposing contacts and the material is extruded side-ways. This collapse mechanism is the same as that produced between two opposite flat punches indenting a sheet of material. For simplicity the triangle *abc* is assumed to be an isosceles right-angle triangle and *bcd* is assumed to be isosceles triangle with the length of side *bd* equal to that of *bc*. The collapse mechanism D has a single degree of freedom specified by the angle ϕ, as shown in the Fig. 10; a typical velocity field is included in the figure. The local collapse pressure at the contact is obtained by equating the rate of external work to the rate of internal plastic work dissipation, given by the equation

$$\frac{p_2}{2k} = \frac{l_{12}v_{12} + l_{24}v_{24} + l_{23}v_{23} + l_{34}v_{34}}{2a_2v_1} + \frac{p_1}{2k}\frac{a_1}{a_2}\frac{v_4}{v_1}, \tag{16}$$

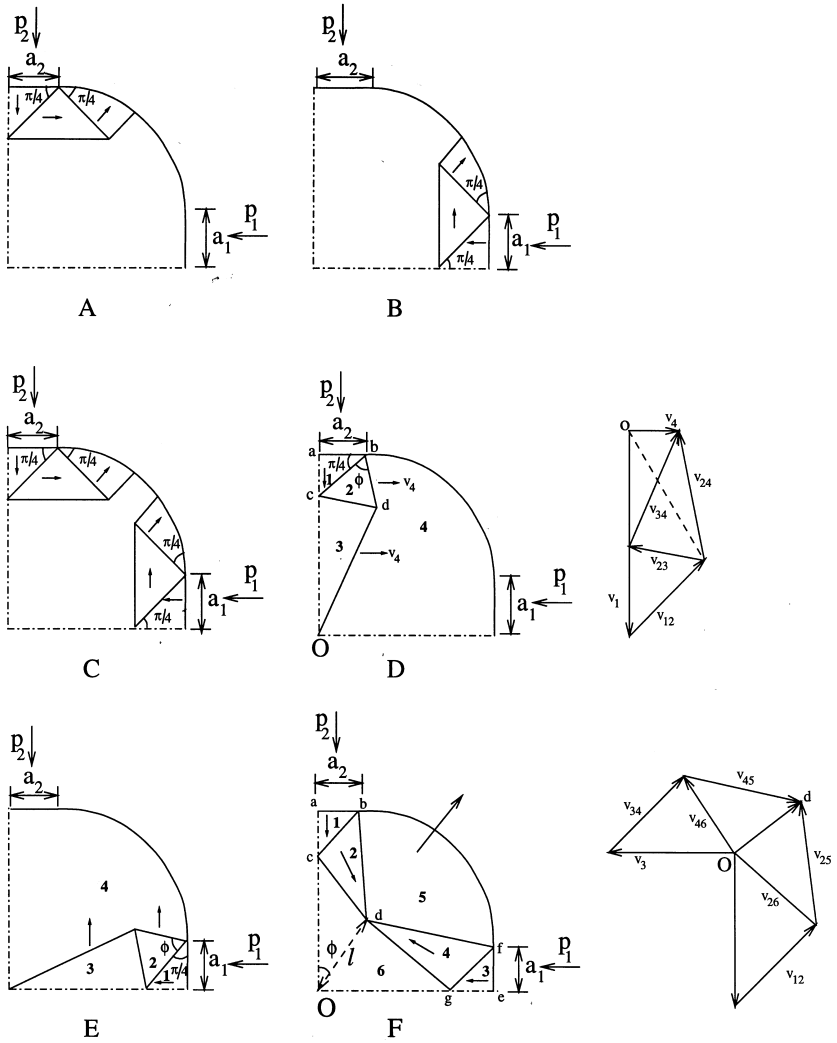

Fig. 10. Upper bound collapse mechanisms for a square array of cylindrical fibres during probing of the yield surface.

where k is the shear yield strength of the material and is equal to $\sigma_Y/\sqrt{3}$ for a von Mises material, l_{ij} denotes the interfacial length and v_{ij} denotes the tangential velocity jump of block i relative to block j. For given values of a_1, a_2 and p_1, the best estimate for p_2 is the least value, obtained by varying the angle ϕ. The process is repeated for other values of p_1 in order to construct the collapse locus in (p_1, p_2) space.

The collapse mode E is the same as D, but with the roles of p_1 and p_2 interchanged. The collapse mechanism F exhibits contact–contact interaction. The material inside the envelope *ocdg* is rigid and stationary, whereas the rigid block outside the region *bdf* moves rigidly outwards. The blocks *abc* and *efg* are assumed to be isosceles right-angled triangles. This interaction mechanism has two degrees of freedom ϕ and l, as shown. For an assumed value of p_1, the best estimate of p_2 is the

minimum value obtained by varying ϕ and l in the equation

$$\frac{p_1}{2k} + \frac{p_2}{2k}\frac{a_2}{a_1}\frac{v_2}{v_1} = \frac{l_{12}v_{12} + l_{25}v_{25} + l_{26}v_{26} + l_{46}v_{46} + l_{34}v_{34} + l_{45}v_{45}}{a_1 v_1}. \tag{17}$$

Repetition of this minimisation procedure for other values of p_1 is used to generate the collapse locus in (p_1, p_2) space. The inner envelope of the locus of contact pressures obtained by each mechanism gives a local yield surface, which can be converted into a macroscopic yield surface using relations (5) and (6). The macroscopic yield surface in Σ_1–Σ_2 space is included in Fig. 9 for relative densities $D = 0.8$ and 0.85 of hydrostatic compacts. When the relative density is 0.8, the yield surface is formed by mechanisms A and B, i.e. Prandtl fields for isolated contacts, and the contact interaction mechanisms D and E. At the higher relative density of 0.85, the increased contact size leads to contact–contact interaction and mechanism F replaces mechanisms A and B as the inner envelope of the yield surface. As expected, the yield surface by the upper bound method encloses that of the slip-line field method. The shapes are similar, except for the local shape at the loading point for $D = 0.8$, see Fig. 9(a); the upper bound method suggests a sharp vertex whereas the slip-line field method gives a smooth yield surface in the vicinity of the loading point.

4.3. Finite element approach

The finite element method has also been used to calculate the yield surface following Stage I compaction for an elastic, ideally plastic powder. The unit cell of the powder particle array was first compacted to the required relative density, and then unloaded elastically to almost zero macroscopic stress. The limit yield surface of the compact at this relative density was determined by reloading the compact along various stress and strain paths until it yields; the values of the macroscopic stresses Σ_1 and Σ_2 at limit yield are used to obtain the yield surface. The reloading paths comprise the proportional stress path of unconstrained uniaxial compression, and a number of proportional strain paths given by $\delta E_1 = \delta E_2 \tan(\psi)$, where δE_1 and δE_2 are strain increments, and the phase angle of loading ψ is kept constant throughout reloading.

The macroscopic yield surfaces obtained by the finite element method are shown in Fig. 9 for hydrostatic compacts of relative densities $D = 0.8$ and 0.85. The finite element results have a pronounced corner on the yield surface at the loading point. In contrast, the slip-line field solution at both values of relative densities (and the upper-bound solution at $D = 0.85$) display no such vertex, with contact–contact interaction leading to a smooth surface along the hydrostatic axis. The yield surfaces obtained by FE calculations at both relative densities ($D = 0.8$ and 0.85) lie within those predicted by slip-line field and upper bound methods. The differences between the finite element and slip-line field solutions are due to (i) slight differences in the assumed geometries, (ii) the fact that the full family of slip-line field solutions may not have been determined, and (iii) the numerical errors associated with the calculation of slip-line field results. We conclude that the finite element results are the most accurate of the three methods adopted.

4.4. Stage I yield surface for a random distribution of particles

So far, we have considered the plastic response of a regular array of cylindrical particles. The question arises, does the response change significantly for a random array of particles? An upper

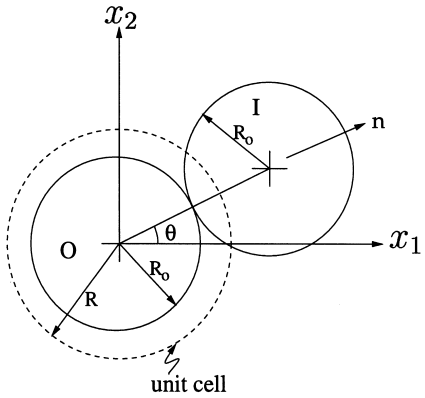

Fig. 11. Typical contact between two cylindrical particles, for the random particle upper bound method.

bound method now described is used to estimate the 2D macroscopic yield surface for a random distribution of cylindrical rigid-perfectly plastic particles, as described by Fleck et al. [8] and Fleck [5] for the 3D case. A velocity field $v(x)$ is derived throughout the body from a uniform macroscopic plastic strain rate $\dot{E}_{ij}$. The internal plastic dissipation rate per unit macroscopic volume $\dot{W}$ is calculated from the assumed velocity field, with the macroscopic stress Σ_{ij} derived from the plastic dissipation rate per unit volume, as discussed by Gurson [23]. That is,

$$\Sigma_{ij} = \frac{\partial \dot{W}}{\partial \dot{E}_{ij}}, \tag{18}$$

where $\dot{E}_{ij}$ is the macroscopic strain rate.

Consider a typical contact between neighbouring cylindrical powder particles each of radius R_0 as shown in Fig. 11. The relative velocity v_i of particle I with respect to the stationary reference particle O is taken to be

$$v_i = \dot{E}_{ij} n_j 2R_0, \tag{19}$$

where **n** is the unit normal vector from the centre of particle O to the centre of particle I, and x_i is a Cartesian reference frame as defined in Fig. 11. The velocity v_i can be resolved into the normal component $v_n(\theta)$ and the tangential component $v_t(\theta)$ at the contact between the two particles. Within Stage I compaction regime, plastic dissipation is limited to the vicinity of the contact. As the particles are assumed to be frictionless, zero shear traction is supported across the contact; the average normal pressure between the contacts is written as p_c. Let Z the number of contacts per particle ($Z = 4$ for the case of square array of cylindrical particles) and let A_c be the average contact area. The plastic dissipation per contact is

$$\dot{W}_c(\theta) = p_c A_c \frac{v_n}{2}. \tag{20}$$

The factor of 2 in the denominator is due to the fact that plastic dissipation is shared between two particles at each contact and so half is apportioned to each particle. The average plastic dissipation

per particle is

$$\dot{W}_p = \frac{1}{2\pi R_0}\int_{S_0} Z\dot{W}_c \,\mathrm{d}s, \tag{21}$$

where the integration is carried out over the surface area of particle O. The plastic dissipation per unit macroscopic volume $\dot{W}$ is obtained by multiplying the average plastic dissipation per particle by D/V_p, where V_p is the volume of each particle. Thus,

$$\dot{W} = \frac{D}{2\pi R_0}\int_{S_0} \frac{Z\dot{W}_c}{\pi R_0^2}\,\mathrm{d}s \tag{22}$$

$$= \frac{2D}{\pi}\int_0^{\pi/2} \frac{Zp_cA_cV_n}{2\pi R_0^2}\,\mathrm{d}\theta. \tag{23}$$

Recall that the relative density D for an isostatically pre-compacted specimen is related to the normalised contact width a/b by Eq. (12). The assumed collapse mechanism is the slip-line field for Stage I hydrostatic compaction as described in Section 3.2. The collapse pressure is given by $p_c = \sigma_Y f(a/b)$, where f is a dimensionless function of a/b. For $a/b < 0.11$, the Prandtl field solution pertains for the isolated contact and $f \equiv 2.97$. When a/b exceeds 0.11, contact–contact interaction occurs and f drops in value.

For a given macroscopic strain rate $(\dot{E}_1, \dot{E}_2)$, the normal component of velocity v_n is given by

$$v_n(\theta) = (\dot{E}_1\cos^2\theta + \dot{E}_2\sin^2\theta)2R_0. \tag{24}$$

Analytical expressions for the yield surface follows by substituting Eq. (24) into Eq. (23) and then evaluating Eq. (18).

For the case $\dot{E}_1 < 0$ and $\dot{E}_2 < 0$, the macroscopic stresses are given by

$$\Sigma_1 = \Sigma_2 = -\frac{1}{2}\frac{Zp_cA_cD}{\pi R_0}. \tag{25}$$

Upon introducing the loading angle $\theta_c \equiv \tan^{-1}(\sqrt{-\dot{E}_1/\dot{E}_2})$, the macroscopic stresses are given by

$$\Sigma_1 = -\frac{D}{\pi}\frac{Zp_cA_c}{2\pi R_0}(\pi - 2\theta_c - \sin 2\theta_c), \tag{26}$$

$$\Sigma_2 = -\frac{D}{\pi}\frac{Zp_cA_c}{2\pi R_0}(\pi - 2\theta_c + \sin 2\theta_c) \tag{27}$$

for $\dot{E}_1 > 0$ and $\dot{E}_2 < 0$, and by

$$\Sigma_1 = -\frac{D}{\pi}\frac{Zp_cA_c}{2\pi R_0}(2\theta_c + \sin 2\theta_c), \tag{28}$$

$$\Sigma_2 = -\frac{D}{\pi}\frac{Zp_cA_c}{2\pi R_0}(2\theta_c - \sin 2\theta_c) \tag{29}$$

for $\dot{E}_1 < 0$ and $\dot{E}_2 > 0$. The assumption of zero cohesive strength between particles leads directly to the result $\Sigma_1 = \Sigma_2 = 0$ for both $\dot{E}_1 > 0$ and $\dot{E}_2 > 0$.

Eq. (25) shows that for a wide range of strain rate directions ($\dot{E}_1 < 0$ and $\dot{E}_2 < 0$) the macroscopic stress lies at a vertex on the hydrostatic stress axis, labelled V in Fig. 9(a). In this figure, the curve OXV is represented by Eqs. (26) and (27) and the curve OWV is represented by Eqs. (28) and (29). The yield surface is almost flat on each side of the vertex, and can be represented to fair accuracy by the maximum stress criterion

$$\mathrm{Max}(\Sigma_1, \Sigma_2) = -\frac{1}{2}\frac{Zp_cA_cD}{\pi R_0}. \tag{30}$$

Gurson [23] has shown that the macroscopic strain rate $\dot{E}_{ij}$ is normal to the yield surface $\Phi(\Sigma)$ when the yield surface is calculated by such an upper bound approximation. Thus, the strain rate vector with components $(\dot{E}_1, \dot{E}_2)$ is normal to the yield surface. Consequently, plastic flow in the vicinity of the vertex is closely aligned with the direction of the largest principal stress with little or no straining in the other directions. That is, if Σ_1 or Σ_2 is the stress causing yielding, the plastic strain rate is almost uniaxial. However, when yield occurs at the vertex with $\Sigma_1 = \Sigma_2$, the direction of plastic flow can range from nearly uniaxial straining to purely hydrostatic deformation. We note from Fig. 9(a) that the shape of the yield surface near the vertex for a random distribution of particles is in close agreement with that derived for a square array of particles by the slip-line field, upper bound and finite element methods.

4.5. Yield surface for Stage II hydrostatic compaction

At high relative densities the powder structure can be idealised as a homogeneous compressible elastic–plastic solid with a uniform distribution of cusp-shaped voids. In this section, we construct yield surfaces resulting from hydrostatic compaction to a relative density of 0.95 and 0.98; predictions are compared from the slip-line field method, finite element computations and Gurson's 2D yield surface for the collapse of a circular cylindrical shell [23].

The slip-line fields that exist upon general straining of a unit cell of the hydrostatic precompact in Stage II are shown in Fig. 12. The cusp-shaped void is modelled as a square pore to simplify the slip-line field solutions. The fields G and H are obtained when opposing contacts are loaded more heavily than the neighbouring contacts. This leads to plastic zone interactions between opposing contacts and are similar to the field arising in the forging of a thin sheet with two opposing indenters. The angle of the centre-fan field is determined from the requirement that the outer slip-line must intersect the particle centre at 45°.

Mechanisms I and J are produced when the plastic zone under a contact interacts with the free surface of the adjacent square pore. The angle of the centre-fan is fixed by the condition that it intersects the centre of the contact surface at 45°. The average contact pressure p_2 is determined from the requirement that the net force on the rigid block attached to the square pore is zero.

Mechanism K is the same as the field shown in Fig. 6(c) for Stage II compaction of the square array of particles and is associated with probing along the hydrostatic strain-path $\dot{E}_1 = \dot{E}_2$.

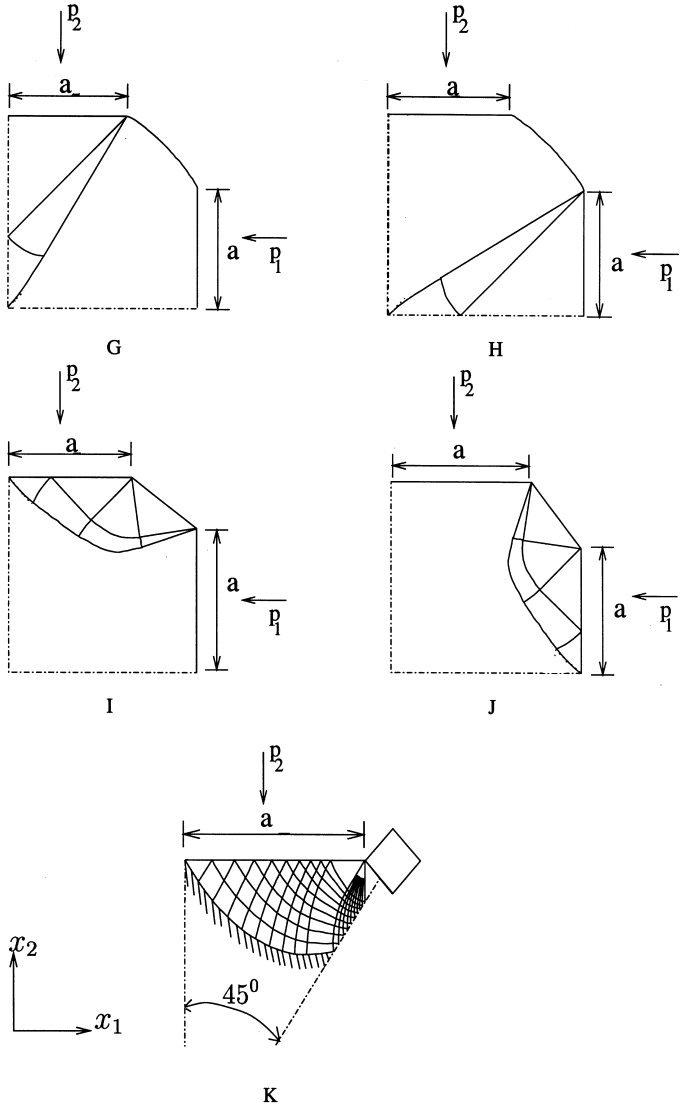

Fig. 12. Slip-line fields for a square array of cylinders during the probing of hydrostatic precompacts ($a_1 = a_2 = a$), in Stage II.

The yield surface from the above slip-line field solutions is compared with that obtained by the finite element method in Fig. 13 for the hydrostatically precompacted specimens of relative densities 0.95 and 0.98. For both values of relative densities, the agreement between the two methods is close despite the fact that a square cylindrical pore is assumed in the slip-line field calculations and a four-sided cusped pore is developed within the finite element simulation. In addition, the Gurson [23] yield surface for circular cylindrical voids is displayed in Fig. 13. Gurson [23] has obtained a yield function of the following form for plane strain deformation of a circular

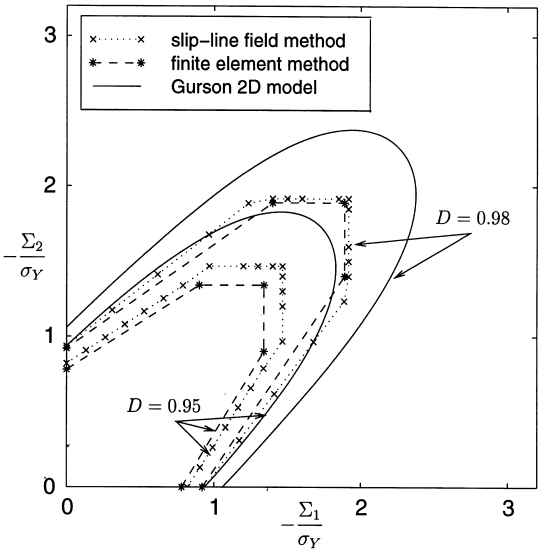

Fig. 13. The macroscopic yield surfaces for hydrostatic precompacts of relative densities $D = 0.95$ and 0.98. Finite element results are compared with the yield criterion of Gurson [23] and slip-line field solutions.

unit cell containing a circular cylindrical void,

$$\Phi_g(\Sigma_m, \Sigma_e, \sigma_Y) = C_{eqv}\left(\frac{\Sigma_e}{D\sigma_Y}\right)^2 - 2\left(\frac{1-D}{D^2}\right)\left[1 - \cosh\left(\sqrt{3}\frac{\Sigma_m}{\sigma_Y}\right)\right] - 1 = 0, \tag{31}$$

where $C_{eqv} = (4 - 3D + 24(1-D)^6)^2$ is the numerical factor for plane strain loading, $\Sigma_e = \sqrt{3}(\Sigma_2 - \Sigma_1)/2$ and $\Sigma_m = (\Sigma_1 + \Sigma_2)/2$ are the macroscopic effective and mean stresses, respectively, and D is the relative density. Both the mean stress and effective stress are normalised by the uniaxial yield strength σ_Y of the matrix. Gurson's yield surfaces are elliptical in shape and predict a significantly stronger material response than those of the current study. The slip-line field and finite element results give yield surfaces of approximately elliptical shape and predict a corner at the initial loading point, i.e. on the hydrostatic stress axis. The close agreement between the slip-line field solutions and the finite element results indicate that the slip-line fields of Fig. 12 adequately describe the yield surface of a hydrostatically precompacted square array of cylindrical particles in Stage II.

5. General biaxial loading

In this section, the finite element method is used to study the deformation characteristics of the cylindrical particle array for a range of proportional strain paths in macroscopic strain space, given by $\dot{E}_1 = \dot{E}_2 \tan\psi$. The phase angle ψ is kept constant throughout the loading programme. We note in passing that the strain paths $\psi = 0$ and 45° are directly related to the practical production processes of closed-die and isostatic compaction, respectively.

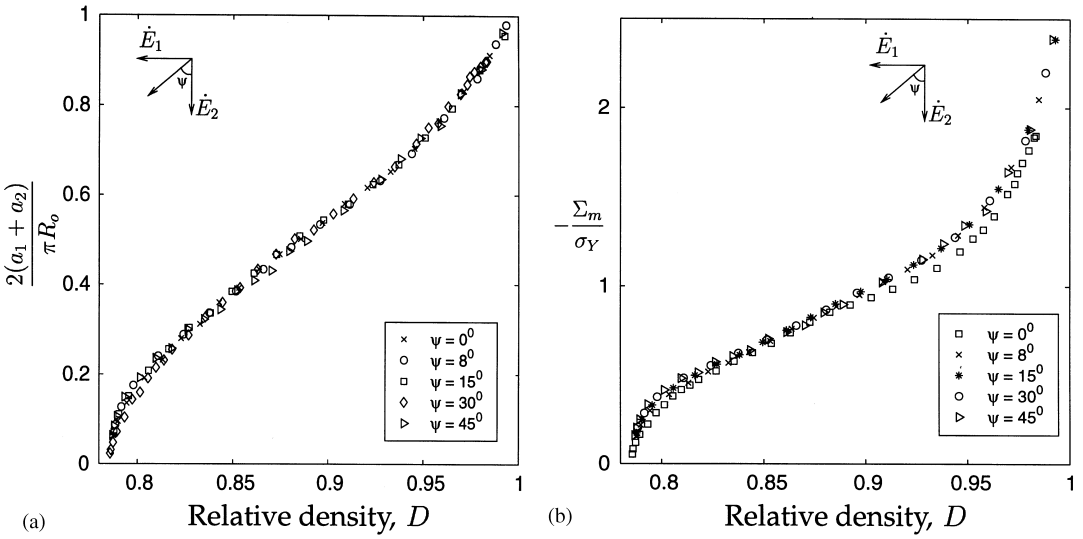

Fig. 14. (a) Evolution of contact width with relative density, for the compaction of a square array of particles subjected to a selection of strain paths. (b) The normalised macroscopic mean pressure $-\Sigma_m/\sigma_Y$ as a function of the relative density D.

5.1. Evolution of contact widths and mean pressure under proportional straining

The vertical and horizontal contacts flatten at different rates under general loading. In Fig. 14(a) the total contact width, normalised by the initial particle perimeter $2\pi R_0$, $4(a_1 + a_2)/(2\pi R_0)$ is plotted against the relative density of the compact. Remarkably, the area of contact is almost independent of the strain path and is primarily a function of the relative density. This 2D result contrasts with the 3D result for a cubic array of spherical particles: Ogbonna and Fleck [13] predict a significantly larger total contact area for isostatic compaction compared with closed-die compaction at a given relative density.

A plot of the macroscopic mean stress $\Sigma_m(= (\Sigma_1 + \Sigma_2)/2)$ as a function of the relative density D for different loading paths is shown in Fig. 14(b). For all strain paths considered, the relative density increases monotonically with increasing mean pressure. Again, the effect of loading phase angle ψ on the macroscopic mean pressure versus density response is minor.

5.2. Local contact pressures and macroscopic stresses

The mean contact pressures at the contact are calculated by dividing the contact load by the contact widths. A plot of the normalised contact pressures p_1/σ_Y and p_2/σ_Y versus the macroscopic strain E_2 are shown in Figs. 15(a) and 15(b), respectively. As for the case of hydrostatic compaction, the normalised contact pressure initially drops due to neighbouring contact–contact interaction (*softening*) and later the mean contact pressure rises due to geometric hardening.

The macroscopic stresses Σ_1 and Σ_2 have been calculated using Eqs. (5) and (6), respectively, and are plotted against the macroscopic strain E_2 in Figs. 16(a) and 16(b) for all the strain paths considered. A continuous increase in the macroscopic stress with densification is predicted.

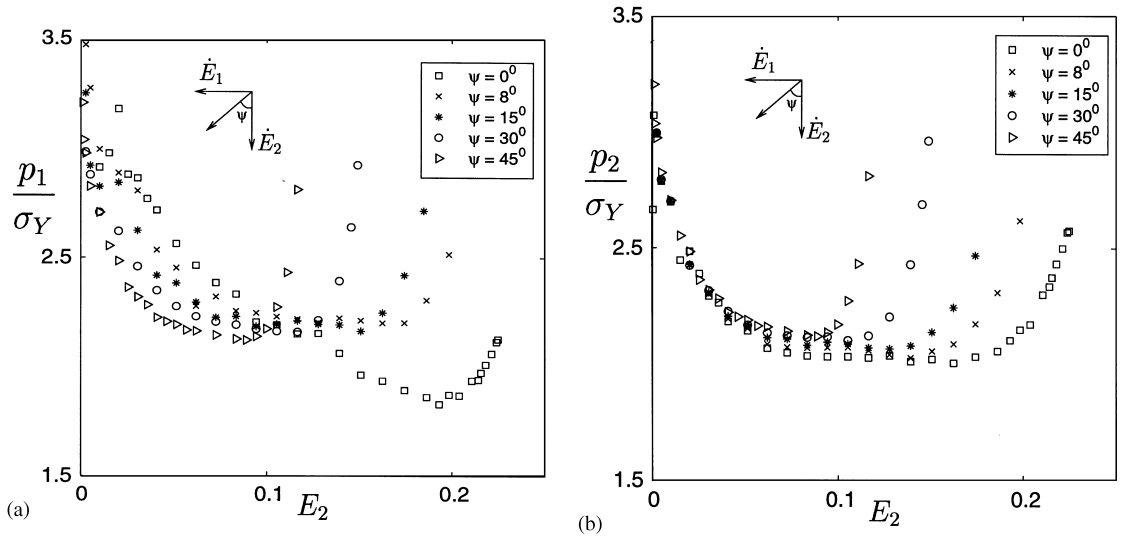

Fig. 15. The evolution of the normalised local contact stress: (a) p_1/σ_Y; and (b) p_2/σ_Y with true strain E_2, for a selection of macroscopic strain paths.

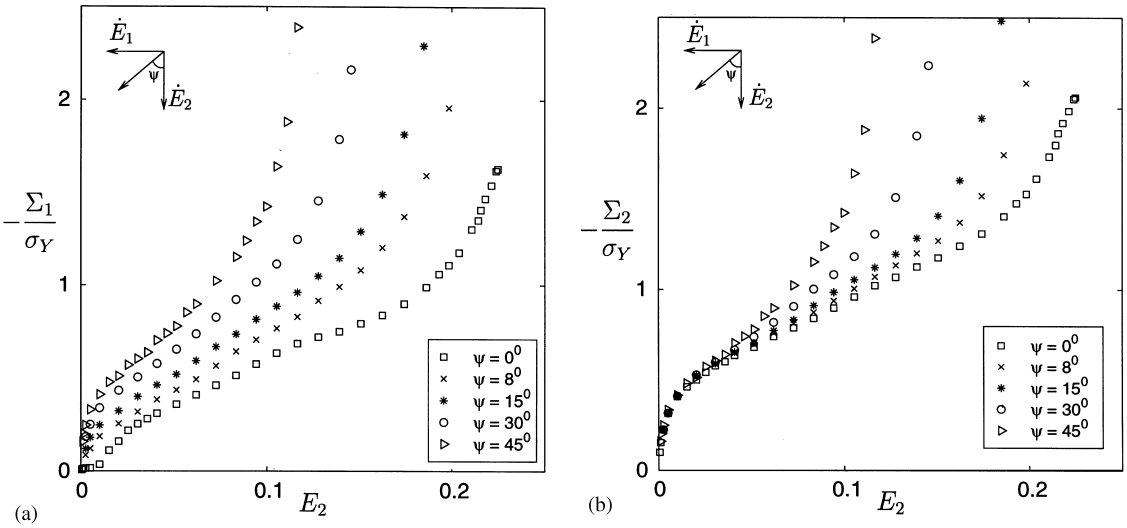

Fig. 16. The evolution of normalised macroscopic stress: (a) $-\Sigma_1/\sigma_Y$; and (b) $-\Sigma_2/\sigma_Y$ with true strain E_2, for a selection of macroscopic strain paths.

6. Yield surface for closed-die compaction

In this section we explore the yield surface due to closed-die compaction along the x_2-direction (with $E_1 = 0$) by making use of the same methodology as that employed above for hydrostatic

compaction. As expected (see Ref. [5]) strong anisotropy develops due to the fact that the contact width a_2 increases more rapidly than a_1 with increasing relative density.

6.1. *Stage I* ($0.785 \leqslant D \leqslant 0.87$)

The relevant slip-line fields have already been presented in Fig. 7 to obtain a yield surface. The local yield surfaces in p_1–p_2 space for closed-die compacts of relative density 0.8 and 0.85 are shown in Fig. 8(b). When the relative density is 0.8, the yield surface consists of two straight segments. One of them arises from the interaction between opposing contacts between the larger contacts of width a_2, designated mechanism D. The other contact of dimension a_1 is much smaller and there is no other interaction with any other contacts. Consequently, the Prandtl punch field B is activated. Further densification to a relative density of 0.85 results in larger contacts a_1 and a_2. There is now a stronger interaction between top and bottom contacts of dimension a_2, leading to a drop in the contact pressure at yield. For example, at large relative values of p_1 to p_2 yield is by plastic collapse between the contacts of dimension a_1 (mechanism E). This mechanism is superseded by the Prandtl mechanism B only at large p_1 and p_2. By using relations (5) and (6) the local yield surface is converted into a macroscopic one and is presented in Fig. 17(a). For completeness results are included in Fig. 17(a) for the yield surface obtained by the upper bound method for the mechanisms described in Fig. 10 and by the finite element method. The finite element predictions for the yield surfaces taken as the reference solutions; however, the three solutions are in good agreement, and differences can be largely attributed to the fact that the assumed geometry is slightly different in each case. A vertex is present at the initial loading point according to all three solution methods.

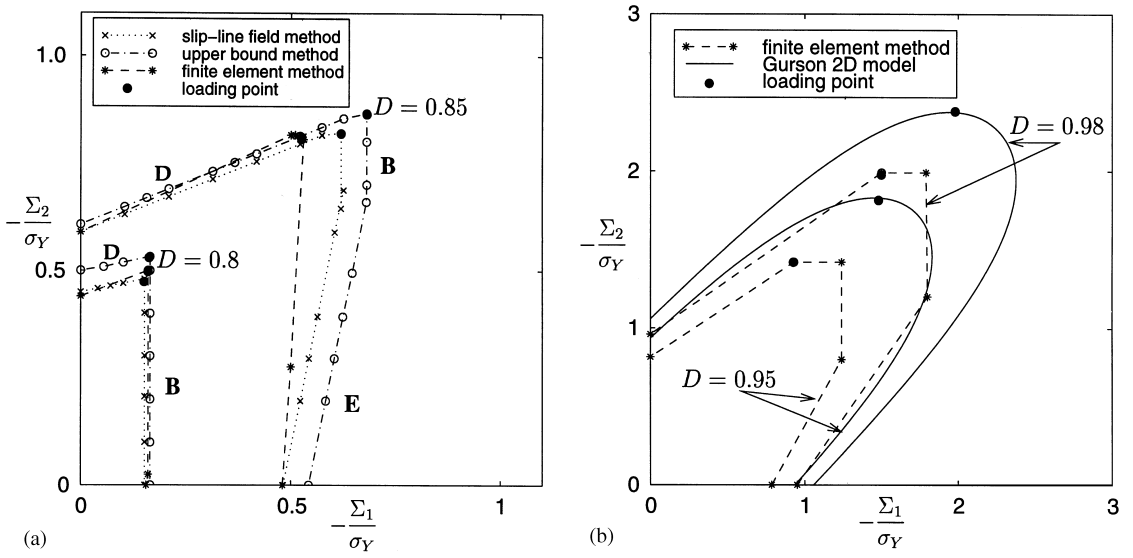

Fig. 17. Comparison of macroscopic yield surfaces generated by various methods, due to closed-die compaction: (a) Yield surfaces at $D = 0.8$ and 0.85, by the slip-line field, upper bound and finite element methods; (b) Yield surfaces at $D = 0.95$ and 0.98, by the finite element method and according to the Gurson 2D model [23].

Closed-die compaction along the x_2-direction results in contacts of size a_2 which are larger than those obtained by hydrostatic compaction to the same relative density, while the contacts of size a_1 normal to the x_1-axis are smaller. This results in a stretching of the yield surfaces in the direction of straining and a contraction in the transverse direction compared to the yield surfaces for hydrostatic compaction. This demonstrates that the yield behaviour of the powder compact is not just a function of the relative density, but also of the deformation path. This path-dependent yield behaviour can be used to produce components with directional properties.

6.2. *Stage II* ($0.906 \leqslant D \leqslant 1$)

The finite element method has been used to determine the yield surface due to closed-die compaction in Stage II regime. The resulting yield surfaces for the closed-die precompacts of relative density $D = 0.95$ and 0.98 are shown in Fig. 17(b) and are compared with Gurson's 2D yield surface for the collapse of a circular cylindrical shell [23]. The finite element predictions reveal that the yield surface for a square array of particles consists of a series of flats, with the loading point for closed-die compaction laying on the horizontal flat. The existence of these straight line segments has been confirmed by probing the yield surface over a large number of strain rate directions. In contrast, Gurson's yield surface is smooth, and is slightly larger than the one for a square array of particles for the given values of relative density. These differences in yield surface shape are not surprising: the finite element analysis addresses a simple square array of particles whereas the Gurson model implicitly assumes a random distribution of voids.

The finite element predictions for the yield surface evolution after hydrostatic and closed-die compaction are summarised in (Σ_1, Σ_2) space in Fig. 18(a), for both Stages I and II. It is noted that

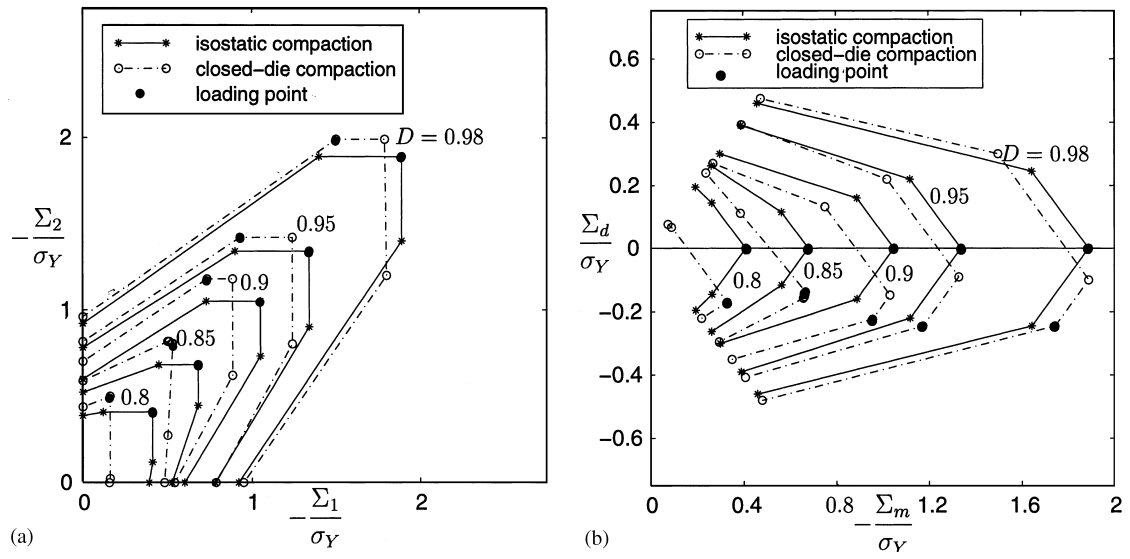

Fig. 18. Comparison of the macroscopic yield surfaces after closed-die compaction and hydrostatic compaction: (a) Σ_1 versus Σ_2 space; (b) deviatoric stress $(\Sigma_1 - \Sigma_2)/2$ versus mean stress $(\Sigma_1 + \Sigma_2)/2$ space.

with progressive densification the degree of anisotropy associated with closed-die compaction decreases. It is instructive to replot these yield surfaces using axes of mean stress, $\Sigma_m = (\Sigma_1 + \Sigma_2)/2$ and deviatoric stress, $\Sigma_d = (\Sigma_1 - \Sigma_2)/2$, see Fig. 18(b). The shape of the resulting yield surfaces may be approximated by a quadratic function of deviatoric and mean stress, in support of several phenomenological models as reviewed by Doraivelu et al. [3]. The path dependence of yield surface shape is again evident, with the yield surface rotated along the direction of the loading vector.

7. The significance of strain hardening

Finally, the effect of strain hardening is explored for both hydrostatic and closed-die compaction of the square array of cylindrical particles. The matrix is taken as an isotropic hardening J2 flow theory solid, with a uniaxial stress–strain law given by

$$\begin{aligned} \frac{\varepsilon}{\varepsilon_Y} &= \frac{\sigma}{\sigma_Y} \qquad \text{for } \sigma \leqslant \sigma_Y, \\ &= \left(\frac{\sigma}{\sigma_Y}\right)^{1/N} \qquad \text{for } \sigma > \sigma_Y. \end{aligned} \tag{32}$$

Here, σ_Y is the initial yield stress corresponding to a yield strain $\varepsilon_Y = \sigma_Y/E$, where E is Young's modulus. The strain-hardening exponent N is assumed to be in the range $0 \leqslant N \leqslant 1$, with $N = 0$ describing an elastic-perfectly plastic solid. In the simulations, the yield strain ε_Y is chosen to be equal to 10^{-4}, and Poisson's ratio $\nu = 0.3$. The FE mesh of Fig. 2 is used for the computations with the displacements u_1 and u_2 specified in order to give the required strain path.

The normalised macroscopic stress Σ_2 versus the relative density D for various values of strain hardening exponent N, is shown in Fig. 19 for both hydrostatic and closed-die compaction. We conclude that the compressibility of the array decreases with increasing value of the strain-hardening exponent N for both hydrostatic and closed-die compaction. Also for all values of N considered, the value of the macroscopic stress Σ_2 required to attain a given density is higher for closed-die compaction than for hydrostatic compaction. Similar observations have been made by Akisanya and Cocks [15] in their FE work on the compaction of a hexagonal array of cylindrical particles.

8. Concluding remarks

Consider first the case of hydrostatic compaction. The results of slip-line field and finite element calculations indicate that the interaction of plastic deformation between contacts influences the pressure–density response of a regular square array of cylindrical particles. With increasing densification the local contact pressure decreases from the Prandtl punch solution due to contact–contact interaction. This observation is in agreement with the findings of Ogbonna and Fleck [13] for a cubic array of spherical particles, and the findings of Akisanya et al. [12] for a hexagonal array of cylindrical particles.

Slip-line field, upper bound, finite element and random array upper bound methods have been employed to study the yield surface evolution under hydrostatic and closed-die compaction. The

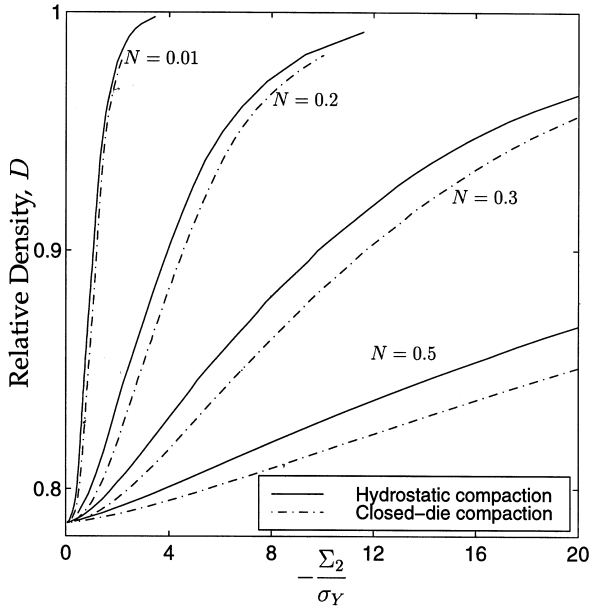

Fig. 19. The effect of strain hardening upon the macroscopic stress to compact a square array of cylinders along a hydrostatic strain path and along a closed-die strain path.

rigid-plastic collapse mechanisms presented represent the yield behaviour reasonably well, (see Figs. 9 and 17). The general shape of the yield surfaces is consistent with the anisotropic model of Fleck [5] and more recently that of Storakers et al. [6] for isolated contacts of spherical particles: the surfaces become elongated in the direction of straining during the initial stages of compaction. With increasing relative density of the precompacts the degree of anisotropy first increases and then decreases again to a response close to that predicted by Gurson [23].

Acknowledgements

The authors are grateful for financial support from NIST, under contract 70-NANB5H0042. ARA acknowledges the financial support of the Nuffield Foundation. IS thanks Cambridge Commonwealth Trust for funding in the form of a research studentship.

References

[1] Ashby MF. HIP 6.0 background reading: the modelling of hot-isostatic pressing. Cambridge University Report, England 1990.
[2] Helle HS, Easterling KE, Ashby MF. Hot-isostatic pressing diagrams: new developments. Acta Metallurgica 1985;33(12):2163–74.

[3] Doraivelu SM, Gegel HL, Gunasekhara JS, Malas JC, Morgan JT. A new yield function for compressible P/M materials. International Journal of Mechanical Sciences 1984;26(9-10):527–35.
[4] Brown BS, Abou-Chedid G. Yield behaviour of metal powder assemblages. Journal of Mechanics and Physics of Solids 1994;42(3):383–99.
[5] Fleck NA. On the cold compaction of powders. Journal of Mechanics and Physics of Solids 1995;43(9):1409–31.
[6] Storakers B, Fleck NA, McMeeking RM. The viscoelastic compaction of composite powders. Journal of Mechanics and Physics of Solids 1999;47(4):785–815.
[7] Akisanya AR, Cocks ACF, Fleck NA. The yield behaviour of metal powders. International Journal of Mechanical Sciences 1997;39(12):1315–24.
[8] Fleck NA, Kuhn LT, McMeeking RM. Yielding of metal powder bonded by isolated contacts. Journal of Mechanics and Physics of Solids 1992;40:1139–62.
[9] Green AP. The plastic yielding of metal junctions due to combined shear and pressure. Journal of Mechanics and Physics of Solids 1954;2:197–211.
[10] Laptev AM, Ul'yanov AN. Deformation of spherical particles during the densification of an idealized porous material I-Investigation of kinematic characteristics. Soviet Powder Metallurgy and Metal Ceramics 1984;23(4):183–6.
[11] Timothy SP, Pearson JM, Hutchings IM. The contact pressure distribution during plastic compression of lead spheres. International Journal of Mechanical Sciences 1987;29(10-11):713–9.
[12] Akisanya AR, Cocks ACF, Fleck NA. Hydrostatic compaction of cylindrical particles. Journal of Mechanics and Physics of Solids 1994;42(7):1067–85.
[13] Ogbonna N, Fleck NA. Compaction of an array of spherical particles. Acta Metallurgica et Materialia 1995;43(2):603–20.
[14] Kunze JM, Wadley HNG. The densification of metal coated powders. Acta Metallurgica et Materialia 1997;45(5):1851–65.
[15] Akisanya AR, Cocks ACF. Stage I compaction of cylindrical particles under non-hydrostatic loading. Journal of Mechanics and Physics of Solids 1995;43(4):605–36.
[16] Wadley HNG, Davison TS, Kunze JM. Densification of metal coated fibres by elastic–plastic contact deformation. Composites B: Engineering 1997;28B(3):233–42.
[17] Fischmeister HF, Arzt E. Densification of powders by particle deformation. Powder Metallurgy 1983;26(2):82–8.
[18] Johnson W. Indentation and forging and the action of Nasmyth's anvil. Engineer 1958;205:348–50.
[19] Johnson W, Mellor PB. Engineering plasticity. New York: Van Nostrand Reinhold Company Limited, 1973.
[20] Gampala R, Elzey DM, Wadley HNG. Plastic deformation of asperities during consolidation of plasma sprayed metal matrix composite monotape. Acta Metallurgica et Materialia 1994;42(8):3209–21.
[21] Mesarovic SD, Fleck NA. Frictionless indentation of dissimilar elastic–plastic spheres. International Journal of Solids and Structures; 37(46-47):7071–91.
[22] Johnson W, Sowerby R, Haddow JB. Plane-strain slip-line fields: theory and bibliography. London: Edward Arnold (Publishers) Ltd., 1970.
[23] Gurson AL. Continuum theory of ductile rupture by void nucleation and growth: Part 1 — Yield Criterion and flow rules for porous ductile media. Transactions of ASME Journal of Engineering Materials Technology 1977;99(1):2–15.